Smart Structures and Systems, *Vol. 33*, *No. 1* (*2024*) *41-53*
https://doi.org/10.12989/sss.2024.33.1.041

Experimental and numerical validation of guided wave based on time-reversal for evaluating grouting defects of multi-interface sleeve

Jiahe Liu [1a], Li Tang [2], Dongsheng Li*[3] and Wei Shen [4]

[1] *School of Civil Engineering*, *Dalian University of Technology*, *Dalian*, *116024*, *China*
[2] *School of Electrical Engineering, University of South China, Hengyang, 421001, China*
[3] *State key Laboratory of Coastal and Offshore Engineering, Dalian University of Technology, Dalian, 116024, China*
[4] *College of Civil Engineering and Architecture, Guangxi University, Nanning, 530004, China*

(*Received March 23*, *2022*, *Revised December 8*, *2023*, *Accepted December 22*, *2023*)

Abstract. Grouting sleeves are an essential connecting component of prefabricated components, and the quality of grouting has a significant influence on structural integrity and seismic performance. The embedded grouting sleeve (EGS)'s grouting defects are highly undetectable and random, and no effective monitoring method exists. This paper proposes an ultrasonic guided wave method and provides a set of guidelines for selecting the optimal frequency and suitable period for the EGS. The optimal frequency was determined by considering the group velocity, wave structure, and wave attenuation of the selected mode. Guided waves are prone to multi-modality, modal conversion, energy leakage, and dispersion in the EGS, which is a multi-layer structure. Therefore, a time-reversal (TR)-based multi-mode focusing and dispersion automatic compensation technology is introduced to eliminate the multi-mode phase difference in the EGS. First, the influence of defects on guided waves is analyzed according to the TR coefficient. Second, two major types of damage indicators, namely, the time domain and the wavelet packet energy, are constructed according to the influence method. The constructed wavelet packet energy indicator is more sensitive to the changes of defecting than the conventional time-domain similarity indicator. Both numerical and experimental results show that the proposed method is feasible and beneficial for the detection and quantitative estimation of the grouting defects of the EGS.

Keywords: grouted sleeve; guided wave; multi-layer structure; wavelet packet; time-reversal

1. Introduction

In recent years, precast concrete technology has made significant progress that has improved the construction efficiency of each building component and compensated for the shortcomings of on-site construction (Wu *et al*. 2016). The embedded grouting sleeve (EGS) is an excellent key for the fabricated building (Tullini and Minghini 2016). The defects of the EGS, such as the fullness of grouting that can affect an entire buildings' health and safety, have therefore attracted considerable concern. Such connection-related defects can cause severe losses in extreme situations, even including the entire property (Yao *et al*. 2021). The fullness of grouting is subjected to highly variable factors that combine with neglect of management, extensive construction, ineffective supervision, and the effects of the low refinement degree of construction (Li *et al*. 2019, Ma *et al*. 2019, Xue *et al*. 2021). The defects of grouting hidden inside the EGS make them undetectable. A non-destructive, real-time, and in-situ measure can be most helpful for the entire building if the damage can be detected. Hence, an online debonding monitoring and evaluation technique for the EGS is worth developing.

Various researchers have suggested numerous methods for evaluating grouting defects, and these methods are roughly divided into destructive and non-destructive testing. Destructive detection methods, such as embedding damping sensors, judge the fullness of the grouting according to the damping amplitude (Yao *et al*. 2021). Destructive methods cause some damage to the sleeve and the sensor. Therefore, non-destructive testing methods should be given priority. An acoustic emission (AE) technique can monitor the damage evolution by analyzing the stress wave characteristics released during interfacial bond failure (Ma *et al*. 2019). When AE technology is applied to the defect detection of sleeve compactness of prefabricated components, it is susceptible to environmental noise interference because the sensor is attached to the concrete surface (Li *et al*. 2021). The AE energy signal is superior in concrete strength and sleeve type but not very sensitive to the defects of the grouting material. Penetrating gamma and X-rays provide images of the variation in the thickness of distribution of defect images and accurate dimensional measurement (Zhang *et al*. 2020). However, these methods of debonding monitoring require radiation safety measures (Xue *et al*. 2021). developed an inspection method based on stress wave measurement for defect detection of fully grouted and semi-grouted sleeves. The results showed that stress wave measurement is sensitive to grouting defect

*Corresponding author, Ph.D., Professor,
E-mail: lidongsheng@dlut.edu.cn
[a] Ph.D. Student, E-mail: 1104060917@mail.dlut.edu.cn

ISSN: 1738-1584 (Print), 1738-1991 (Online)

size. But this method requires multiple sensors and does not place the grouted sleeve into the precast structure. Phased array ultrasound technology can be used to image the internal structure and defects of the grouting sleeve, and obtain high-resolution images of the cross-sections (Liu *et al*. 2021). However, this method typically involves an array of multiple sensors, which depends on the sensor density and incurs a high cost. The research on the above techniques provides ideas for grouting defect monitoring. However, the requirements of real-time, high-precision, and quantitative descriptions of the EGS are still difficult to meet.

This paper reports a study on an in-service defect monitoring method for EGS that utilizes ultrasonic guided waves because of their remarkable properties of high accuracy, fast propagation, excitation convenience, and inexpensive implementation (Mitra and Gopalakrishnan 2016, Zhang *et al*. 2019). The method can be potentially developed into a real-time debonding monitoring and assessment tool for large-scale concrete structures. The generation of guided waves requires specific boundary conditions, like tube, cylinder, or plate (Zheng *et al*. 2019). In the case of a cylinder-like EGS, these guided waves include the longitudinal, bending, and torsional modes. They have become a promising candidate for structural health monitoring (SHM) due to their high sensitivity to even structural damages (Guan *et al*. 2017, El Najjar and Mustapha 2020). When assessing damage, the attenuation coefficent defined based on the amplitude of the guided wave signal, the guided wave modal velocity, and the peak value of the spectrum after Fourier transform, and nonlinear parameter have become essential parameters (De Barros *et al*. 2004).

Nevertheless, the guided wave is currently only used in components with simple waveguide structures. If a very complex multi-layer structure is detected, grouting detection will be difficult to achieve as the attenuation, multi-mode, and dispersion of guided waves. Guided wave technology has successfully detected the grouting fullness of a single sleeve (Li and Liu 2019), but the sleeve has not been placed into concrete, thereby lacking in practical guidance. When guided waves propagate along pure steel, only the steel material's attenuation is considered. Nevertheless, for structures that have multi-layer mediums, such as EGS, the phase velocity of the guided wave in the steel bar is higher than the shear, and the longitudinal velocity of the surrounding medium has a high attenuation effect on the propagation of the guided wave along the steel bar (Beard *et al*. 2003, Sun and Zhu 2020). Given these guided waves' limitations, some researchers have developed multi-mode suppression techniques and modal separation analysis (Hay and Rose 2002, Xu *et al*. 2012, Zhu *et al*. 2018). However, they are usually suitable only in situations where the number of guided wave modes is small, and accurate prior information is required. Therefore, it is challenging to apply to the EGS structure. However, time reversal (TR) technology can be used for guided wave multi-mode focusing and automatic dispersion compensation and does not require any prior information (Saitoh and Ishiguro 2021). Thus, this technology can be used in EGS structures to overcome the adverse effects of multi-modality and dispersion phenomena.

TR technology can be automatically focused on solving the two problems of complex sensor and signal processing in the application of guided waves for multi-layer structures. In the ultrasound field, Ing and Fink (1998) first proposed the concept of TR. Since then, the TR method has been widely used in guided wave damage identification and has achieved good results in plate inspection (Mustapha *et al*. 2012, Wang *et al*. 2015). Sutin *et al*. (2003) employed the concept of TR to apply the inelastic properties of cracks, indicating that the TR technique can successfully focus on crack damage location. Qiu and Yuan (2011) used the nonlinear damage TR similarity characteristics in composite material damage detection. When the time-reversed signal passes through the defect, the reconstructed signal will change significantly to evaluate the interface damage of the composite structural material board. In reinforced concrete structures, Mustapha *et al*. (2014) employed the signal obtained by the TR method to construct the similarity damage index of reinforced concrete beams, confirming the effectiveness of the TR method in indetifying reinforced concrete. Hong *et al*. (2016) judged the quality of the bolt connection according to the peak value of the focus point. Du *et al*. (2016) used a real-time quantitative detection method for the depth of pipeline corrosion pits and confirmed that the focus signal based on TR could judge the pipeline corrosion state. However, ultrasonic guided waves based on TR have not been used to analyze the fullness of grouting of the EGS.

This paper proposes an ultrasonic guided wave method based on TR for monitoring and evaluating EGS grouting defects. First, the basic principle of the TR method of guided waves is introduced. Second, a simplified numerical model is proposed, and the model's validity is confirmed. According to the dispersion curve, wave structure, and attenuation coefficient, the optimal frequency and number of cycles of the excitation signal are determined. Then, four EGS specimens with different defect levels are designed, and guided wave monitoring is carried out. Hilbert transform is applied to extract the wave packets of the L(0,9) mode, which is highly sensitive to defects, followed by TR. Finally, an energy similarity indicator is constructed based on the wavelet packet analysis, which need not be compared with the health signal. The numerical simulation and test results based on TR show that the damage can be quantitatively reflected. This paper considers the influence of concrete cover, and proposes developing an efficient non-destructive technique for monitoring grouted sleeve (GS) embedded shear walls, especially in large-scale concrete structures.

2. Proposed methodology

A multi-modal phenomenon occurs in the EGS, and different modes have different wave structures, causing the superposition of signals to change with the size of the grouting defects. This phenomenon makes the evaluation of the EGS grouting defects difficult through the existing

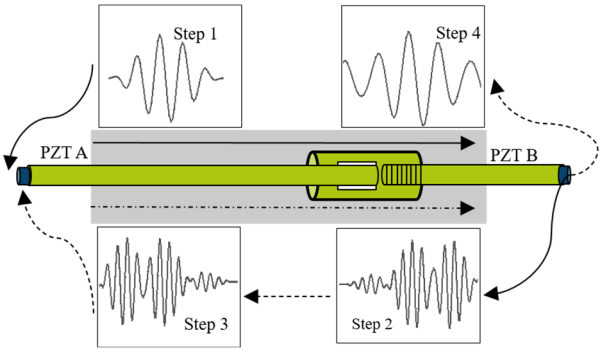

Fig. 1 Time-reversal method of EGS

indicator evaluation. The TR method has been proven to eliminate the influence of multi-modal guided waves, facilitating the assessment of structural damage. The modes of wave can be described as in form of Cartesian notation as (Rose 2014)

$$\rho\frac{\partial^2\mathbf{u}}{\partial t^2}-(\lambda_{\mathrm{L}}+\mu)\nabla(\nabla\cdot\mathbf{u})-\mu\nabla\cdot\nabla\mathbf{u}=\mathbf{0} \tag{1}$$

In the formula, ρ is the density. λ_{L} and μ are the Lame constants. u is the displacement. t is the time. ∇ represents the Hamiltonian operator. Using the stress boundary condition, three modes of guided wave propagation in the cylinder are obtained, namely $\mathrm{L(n,m)}$, $\mathrm{T(n,m)}$ and $\mathrm{F(n,m)}$, where n is related to the geometric characteristics of the cylindrical structure, and m represents the order of the wave. The TR method can be performed because the Eq. (1) only contains even order derivatives, as shown in Fig. 1.

According to Fig. 1, piezoelectric ceramic sheet A receives the N period F frequency signal, the energy of the time domain signal is expressed as E_1, and the frequency domain signal is expressed as $V(\omega)$. Then, piezoelectric ceramic sheet A excites the guided wave to propagate in the sleeve (Step 1).

$$E_1=k_1(\omega)V_1(\omega) \tag{2}$$

where $k_1(\omega)$ is the electromechanical coefficient of PZT A, and the time domain signal of PZT A can be expressed as

$$V_1(t)=\frac{1}{2\pi}\int_{-\infty}^{\infty}V_1(\omega)e^{i\omega t}d\omega \tag{3}$$

The signal transmitted by the guided wave to the PZT B can be expressed as (Step 2)

$$E_2=G(\omega)k_1(\omega)V_1(\omega) \tag{4}$$

where $G(\omega)$ is the transmission coefficient of the sensor path at both ends of the sleeve. The signal received by the PZT B piezoelectric ceramic sheets can be defined as

$$V_2(\omega)=k_2^{-1}(\omega)k_1(\omega)V_1(\omega)G(\omega) \tag{5}$$

The sensors at both ends are from the same factory, and the production models are the same. Thus, the signal can be expressed as

$$V_2(\omega)=V_1(\omega)G(\omega) \tag{6}$$

The time of the $V_2(\omega)$ signal is reversed. According to the time-frequency domain cyclic shift theorem, the time-domain signal turning is equivalent to the frequency-domain conjugate, so the inverted signal can be expressed as

$$V_2'(\omega)=V_1^*(\omega)G^*(\omega) \tag{7}$$

The inverted signal is re-energized by PZT A(Step 3), and the signal received on PAT B is

$$V_2''(\omega)=V_1^*(\omega)G^*(\omega)G(\omega) \tag{8}$$

The guided wave signal received by PZT B is reconstructed as (Step 4)

$$\tilde{V}_2(\omega)==V_1(\omega)G(\omega)G^*(\omega) \tag{9}$$

According to the complex conjugate rule, a complex number is multiplied by its complex conjugate, and the result is a real number

$$G^*(\omega)G(\omega)=Z \tag{10}$$

where Z is the TR coefficient. Therefore, the finally obtained guided wave reconstruction signal can be expressed as

$$\tilde{V}_2(\omega)=ZV_1(\omega) \tag{11}$$

$$\tilde{V}_2(t)=\frac{1}{2\pi}\int_{-\infty}^{\infty}ZV_1(\omega)e^{i\omega t}d\omega \tag{12}$$

If the transmitted signal is unaffected by the frequency, reconstructed signal $\tilde{V}_2(t)$and excitation signal $V_1(t)$ have the same shape. If the transfer function is unaffected by frequency, then the reconstructed signal has the same shape as the excitation signal. However, the transfer function is dependent on frequency, then a big difference will exist between the reconstructed and original signals. The transfer function in a specific mode can be expressed as (Gresil and Giurgiutiu 2015, Huang *et al*. 2018)

$$G(\omega)=A(\omega)\frac{1}{\sqrt{r}}\mathrm{e}^{-\zeta(\omega)r}\mathrm{e}^{-\mathrm{j}k(\omega)r} \tag{13}$$

where $A(\omega)$is mainly affected by the sensor characteristics, the coupling parameters, and the structural response amplitude parameters; $\frac{1}{\sqrt{r}}$ represents the geometric attenuation of the sound wave; $\mathrm{e}^{-\zeta(\omega)r}$ represents the damping attenuation of the sound wave, which is determined by damping $-\zeta(\omega)$, $-\zeta(\omega)$ represents the geometric dispersion of the sound wave. TR coefficient Z is also affected by frequency and damping, which can be expressed as

$$Z=A^2(\omega)\mathrm{e}^{-2\zeta(\omega)r}r^{-1} \tag{14}$$

The above formula shows that TR technology can effectively eliminate geometric dispersion. If the excitation

of guided waves generally uses narrow-band modulation signals, the amplitude parameters and damping can be considered approximately unchanged (Fink 1992, Huang *et al*. 2018). Therefore, the reconstructed and excitation signals are roughly unchanged. However, grouting and concrete materials have a strong dissipative effect. When the ultrasound is in the Rayleigh zone, the scattering attenuation effect of grouting and concrete is approximately positively correlated with the frequency (Philippidis and Aggelis 2005). This phenomenon results in the strong frequency dependence of damping, which destroys the invariance of TR to a certain extent. When grouting defect occurs, the dissipation of guided wave energy is avoided, and the similarity between the reconstructed and original excitation signals increases. This similarity change will provide guidance and suggestions for evaluating the grouting defects in the EGS.

3. Experimental, numerical, and theoretically model

3.1 Experimental setup

A concrete wall that is 750 mm wide, 160 mm deep, and 1000 mm long, as shown in Fig. 2(a), is used in the study. Four half-grouted sleeves with rebars of 18 mm in diameter are embedded within the wall. The rebars are extended outside the concrete by 100 mm on either side of the wall to enable free access to guided waves. Piezoelectric transducers (PZT D33) are used for the excitation and reception of guided waves. The PZT diameter is 18 mm, and the thickness is 15 mm. The PZT is connected to the bayonet nut connector by a dual-core shielded wire. When PZT is used as an exciter or a sensor, it is connected to a signal generator or a data acquisition system. Each PZT is bonded to the rebar end faceby a coupling agent.

A 5-cycle Hanning window with a central frequency of 70 kHz and a peak-to-peak voltage of 9 V, as decipted in Figs. 2(b)-(c), is generated in the function generator and applied to PZT, as expressed in the following equation. The response is received by another PZT using an oscilloscope at the far end of the wall. The output signal is acquired with a sampling frequency of 5 MHz. The complete monitoring process of the guided wave is outlined in Fig. 3.

$$y(t) = v\left[\frac{1}{2}\left(1 - \cos\frac{2\cdot\pi\cdot f\cdot t}{n}\right)\right]\cdot\sin\left(2\cdot\pi\cdot f\cdot t\right) \quad (15)$$

where y(t) represents the voltage excitation, amplitude v takes the value of 9 V, t is the time, f is the center frequency, and n is the number of cycles.

3.2 Grouted sleeve specimens

In this study, to prove the applicability of the proposed detecting method for EGS with guided wave-based TR measurements, half-grouted sleeves that have been widely used in practice are experimentally studied. In prefabricated structures, for column-to-cap and column-to-column joints or wall-to-wall joints, EGS joints are threaded into one end,

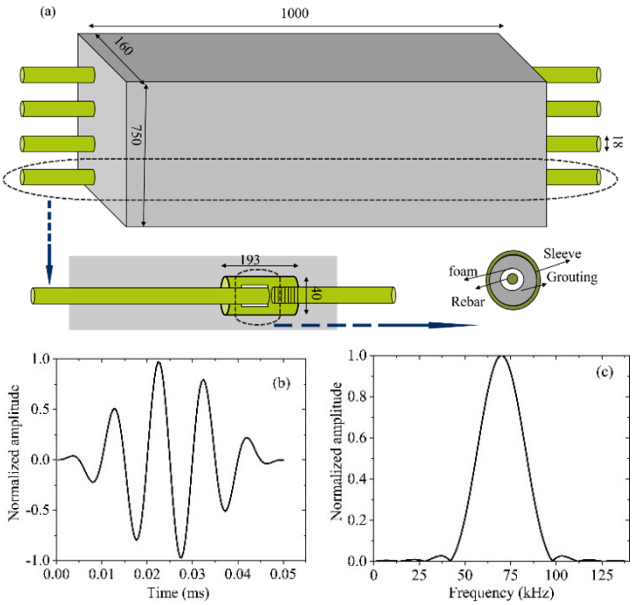

Fig. 2 (a) Schematic diagram of the RC wall; (b) Time-domain of 70 kHz input signal; and (c) Frequency-domain of 70 kHz input signal

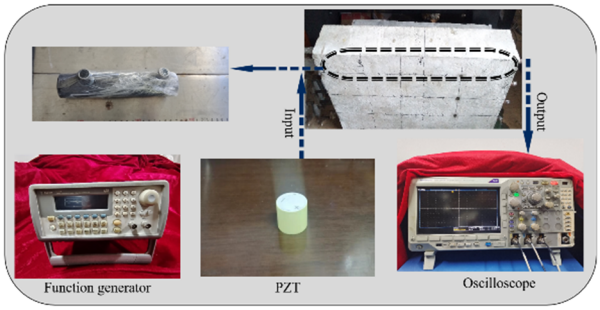

Fig. 3 Guided wave monitoring process diagram

Table 1 Technical parameters of the investigated EGS joints (Unit: mm)

Type length	Inserted Length	Rebar diameter	Sleeve inner diameter	Sleeve outer diameter
GT18	193 144	18	30.5	40

Table 2 Material properties

Type length	Elastic modulus (GPa)	Density (kg/m^3)	Sleeve inner diameter	Dielectric constant in vacuum (C/m)
GT18	200	0.25	7850	-
Steel rebar	200	0.3	7800	-
Grouting material	15.75	0.2	2320	-
Concret	30	0.2	2400	
PZT	-	-	-	8.85E-12

and the other steel is grouted into the opposite end. The key technical parameters of the studied EGS joints are shown in Table 1. The material specifications in the experiment are listed in Table 2. Four EGS specimens with the type of GT18 are investigated. One sample is grouted well, and the other three have different degrees of artificially manufactured grout defects.

3.3 Design of artificially manufactured grout defects in grouted sleeve specimens

The grouting defect of the specimens is manufactured artificially with an ethylene-vinyl acetate (EVA) foam material and compared with one perfect sample. The grout defect types are along the length of the rebar, and the thickness direction remains unchanged for different defect levels, only changing the length direction. EVA polymer foam is uniformly and continuously wrapped on the steel until the outer diameter of the EVA is the same as the inner diameter of the sleeve. Then, the steel is inserted into the GS specimens. The EVA foam material will be gradually filled with the insertion of the grouting material between the sleeve and the steel bar. The EVA foam material can simulate grouting defects very well because of its lightweight, good adhesion, moisture proof, and waterproof advantages. In this paper, the ratio of the length of the EVA foam polymer wrapped steel bar to the size of the inserted steel bar is used as the grout defect degree. The grout defect dimensions of all of the four specimens are decipted in detail in Table 3.

3.4 Numerical and theoretical modeling

In this paper, the finite element analysis software Abaqus/CAE is selected to generate the numerical model of the EGS. Concrete, grouting, sleeve, and steel bars are the different components used, and their properties are shown in Table 2. They are bound by the TIE constraint in the numerical model, which serves as a boundary condition ensuring the continuity of displacement and stress between the rebar, sleeve, and the grout. The defect simulation adopts the elements deletion method, and the analysis type is explicit dynamics. The total simulation time is 1 ms. The mesh dimension should meet at least eight elements for each wavelength, so 1 mm is selected as the mesh dimension. The time step is set to 4E-4 ms to ensure that at least 10-time steps are used in a cycle.

The solution of guided waves propagation along the axial direction in columnar structures has been extensively studied. Interference occurs when waves propagate along the columnar structure. The dispersion curve is a collection of all wave modes that satisfy the condition of constructive interference. For example, the curve can be expressed as the relationship between frequency and phase or group velocity. At present, the dispersion curve can be calculated using the GUIGUW software and PCdisp programs available in the market. The former uses the semi-analytical finite element method and forms a graphical interface with an intuitive operation (Bocchini *et al*. 2011). The latter uses a modal analysis method based on Pochhammer-Chree (PC) theory to solve the behavior of cylindrical waveguides by using MATLAB as the working environment (Seco and Jiménez 2012). The calculation of the dispersion curve of the EGS is very complicated because the geometry of the sleeve, the steel bar, and the concrete wall are different. A previous analysis used the approximate size of the steel bar and considered that the length of concrete is infinite. However, the size of the concrete wall is limited in practice. Thus, if the dimension of the concrete in the wall is finite, the results might be erroneous.

In this study, the cubic concrete geometry is approximately simplified to a cylinder, as decipted in Fig. 4, with an effective radius, R4; the inner sleeve radius, R3; the grouting radius, R2; and the steel bar radius, R1. The value of R4 is taken as the depth of concrete, that is, 80 mm. The properties of the four-layer material are shown in Table 2, which are used to calculate the dispersion curve. The group velocity dispersion curve is generated using a PCdisp program.

Table 3 Material properties

Specimen No.	Defect length (mm)
S1	0 (perfect status)
S2	36
S3	72
S4	108

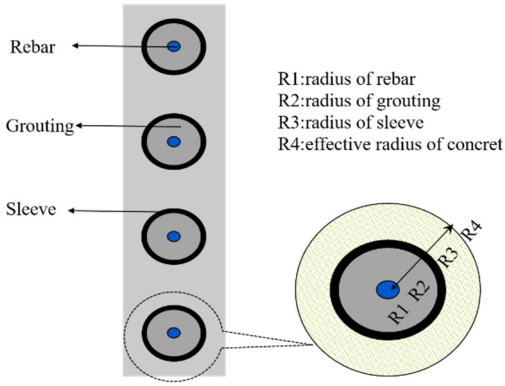

Fig. 4 Approximation of RC wall fabricated for the aim of dispersion curve

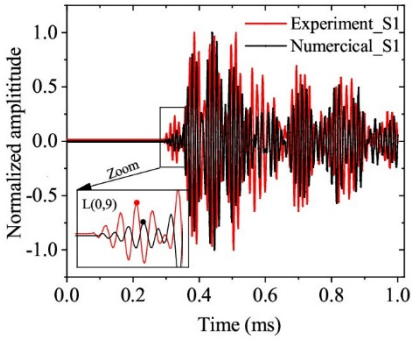

Fig. 5 Comparison of experimental and numerical models in a health state. The dots represent the peaks of the first wave

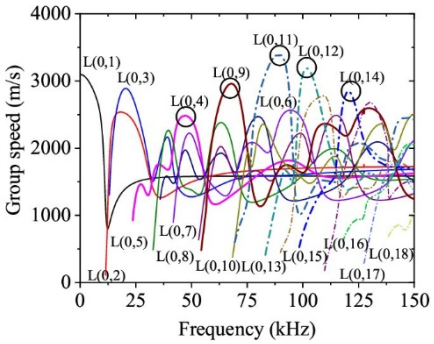

Fig. 6 Group velocity dispersion curves of EGS

The accuracy of the theoretical model in a healthy state is necessary for the damage assessment of structural components. The model under the healthy state is the EGS without grout defects in the numerical simulation. Fig. 5 shows no significant difference in the number of wave packets and the flight time between the experimental and numerical results. It can be seen that due to the experimental equipment and the surrounding environment, the experimental signal will have zero frequency components relative to the numerical signal. The zoomed figure shows that both the experimental and numerical signals show a clear first wave (L(0,9)), which overlaps less with other modes. In addition, the peak values of the first waves of the two are only 4us apart, much smaller than one period of the emitted wave. Therefore, the proposed approximate calculation theoretical model is adequate. The author uses the PCdisp program to calculate the relationship between the group velocity and frequency of the EGS, and the result is shown in Fig. 6.

4. Results and discussion

4.1 Frequency selection

As shown in Fig. 6, the propagation of guided waves in the EGS structure is complex and has many modes. Given that the concrete material wraps the steel bar and is a typical anisotropic material, ultrasonic waves will scatter on its surface. Therefore, the ultrasonic waves in concrete can be divided into three states: the Rayleigh, random, and geometric zones (Planes and Larose 2013). When the wavelength is much smaller than the geometric size and larger than the aggregate size, the wave propagation is in the Rayleigh region. The corresponding frequency range is approximately 20–150 kHz (Kühn *et al*. 2006), and the primary manifestation is interference waves. As the frequency increases to approximately 150 kHz to 1 MHz, the wavelength is equivalent to the size of the concrete aggregate (Fröjd and Ulriksen 2017). The coherent wave decreases, the incoherent wave increases, and the wave is in the random region. When the frequency exceeds 1 MHz, the wave propagation is in the geometric area, and the wave will be severely attenuated, and thus rarely used in practice (Planes and Larose 2013). At present, the application of ultrasound in concrete structures is mainly concentrated in the Rayleigh area. Many experiments and numerical simulations have shown that the attenuation coefficient of sound waves is positively correlated with frequency. The higher the frequency is, the more serious the attenuation will be (Asadollahi and Khazanovich 2019). Therefore, this article also focuses on selecting a guided-wave frequency at 20–150 kHz. In the EGS wave structure, the appropriate frequency will directly affect the evaluation result. The most suitable frequency for EGS grouting defect evaluation is determined from three aspects: group velocity, wave structure, and attenuation coefficient. First, as shown in the group velocity diagram, the group velocity of a single-mode at a specific frequency is significantly greater than that of the other modes, and this point has relatively weak dispersion characteristics. Fig. 6 shows the approximate locations of the five points with the evaluation potential listed below in the Table 4.

Table 4 The choice of the best mode for EGS

Approximate frequency (kHz)	50	70	90	100	120
Mode	L(0,4)	L(0,9)	L(0,11)	L(0,12)	L(0,14)

Second, to clarify the wave structure of these five modes in the EGS, numerical simulation was used to obtain the power flow density across the entire cross-section at the grouting part of the EGS, and the theoretical wave structure is plotted in Fig. 7.

Numerical results and theoretical values are normalized and show a good correlation. These five modes belong to the fastest modes at a specific frequency, but exhibit different wave structures. As shown in Fig. 7, the L(0,4) mode shows that the energy is mainly concentrated in the concrete, which makes it difficult to effectively identify the lack of grouting material. In contrast, the energy of the other four modes is mainly concentrated at the interface between the steel bars and the grouting material, so these four modes are more susceptible to grouting defects. This is because the vibration of the L(0,4) mode mainly occurs in the concrete, and if there is no grouting material, the energy cannot show significant changes in this area. The vibration of the other four modes mainly occurs at the interface between the steel bars and the grouting material, so they are more sensitive to grouting defects. Therefore, 50 kHz is no longer considered as the working frequency. Finally, to find the optimal frequency, the attenuation curve of the received signal is calculated at the remaining four frequencies. The attenuation values of the experimental and numerical results are shown in Fig. 8. The energy attenuation of the received signal is positively correlated with the frequency. For the EGS structure, when the velocity and the wave structure are applicable simultaneously, 70 kHz is selected as the excitation frequency after comparing the attenuation coefficient. Meanwhile, the relatively small frequency also plays a role in reducing the mode.

Narrow-band signals can suppress dispersion to a certain extent (Huang *et al*. 2018). After determining the excitation frequency of the Hanning window, the number of cycles also greatly influences the application of guided waves. The following Fig. 9 shows the signal diagrams of the 5-, and

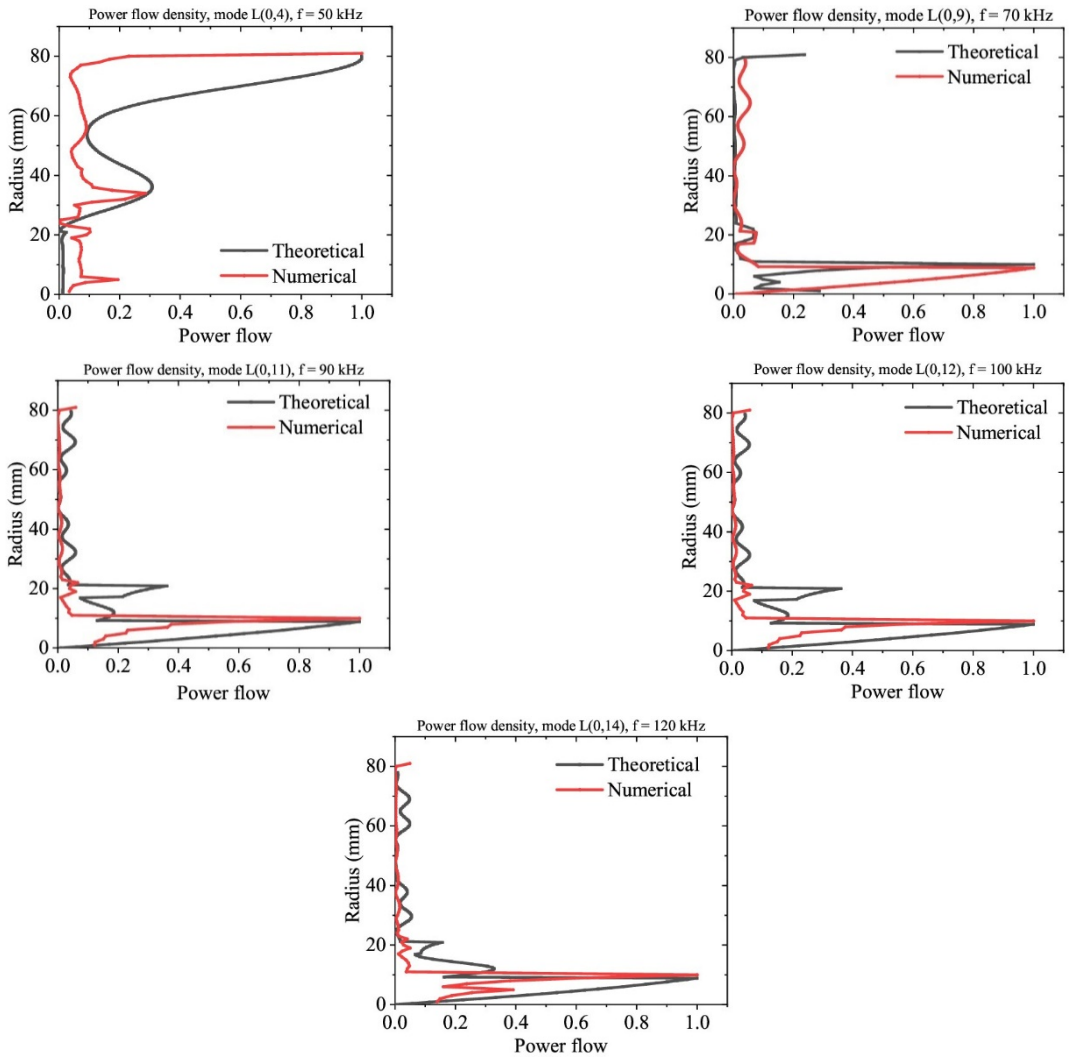

Fig. 7 Power flow density of wave structures for different waveguide modes in theory and numerical analysis

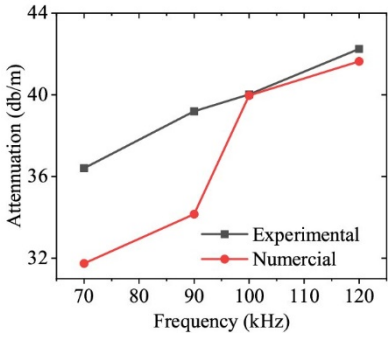

Fig. 8 Test and numerical attenuation curve of the first wave signal

12-period Hanning window modulations at a center frequency of 70 kHz. It can be seen that the higher the number of cycles of the modulation signal is, the more concentrated the frequency spectrum is, suppressing the dispersion phenomenon well. However, the width of the time-domain signal increases with the number of cycles, which will cause the time-domain signals to overlap and the signal uncertainty to be increasingly significant (Su *et al*. 2006). Therefore, spatial and temporal resolutions should be considered in practical applications. Wilcox *et al*. (2001) proposed a minimum resolution dimensionless parameter to compare different operating points. On this Therefore, spatial and temporal resolutions should be considered in practical applications. Besides, this paper proposes a period selection method suitable for a specific model at a particular frequency in the EGS waveguide structure. Under the condition that the frequency spectrum is concentrated, the resolution of the first wave packet is optimized, that is, the minimum period N should meet the following

$$l(v_{\text{sec}}^{-1} - v_{\text{fin}}^{-1}) - Nf^{-1} > 0 \tag{16}$$

where v_{fin} is the speed of the fastest mode of group velocity, v_{sec} is the speed of the group velocity in the second mode, and f is the center frequency of the excitation signal. The theoretical number of cycles should at least satisfy this formula. The difference between the fastest L(0,9) and the next L(0,5) at 70 kHz is approximately 600 m/s, so the calculated N should be less than 6. Therefore, the most suitable excitation signal for the EGS structure is the 70 kHz Hanning window under five cycles.

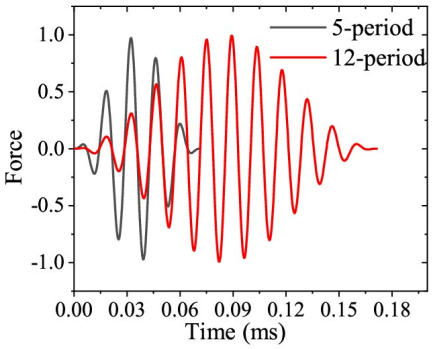

(a) Time domain

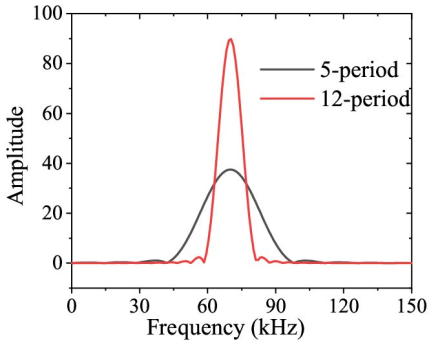

(b) Frequency domain

Fig. 9 Frequency 70 kHz sinusoidal modulation signal diagram under different cycles

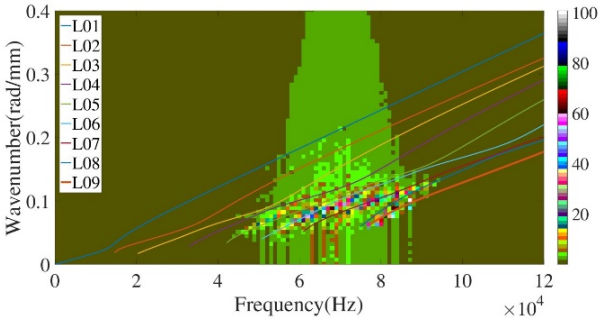

Fig. 10 Frequency wavenumber analysis diagram of EGS structure

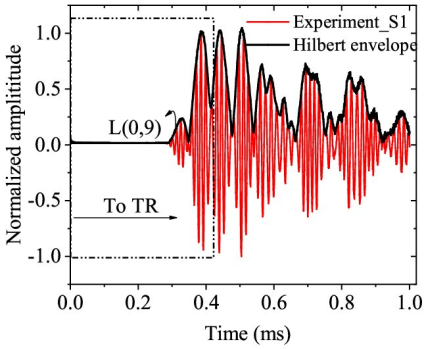

Fig. 11 Schematic diagram of the extraction of the cut-off signal of S1

4.2 Level 2Longitudinal guided waves for detection of EGS

Frequency–wavenumber analysis (2D-FFT) is performed to extract the modal information of the signal (Michaels *et al*. 2011). The wavenumber represents the spatial characteristics of the signal, and frequency refers to the time characteristics of the signal. The primary expression is

$$V(f,k) = \int_{-\infty}^{+\infty} \int_{-\infty}^{+\infty} v(t,x) e^{-j(2\pi ft - kx)} dtdx \qquad (17)$$

where $V(f,k)$ is the value of the signal in the time and space domains, $v(t,x)$ represents the received signal, t is the time data, and x is the spatial data.

Frequency–wavenumber analysis was performed on the steel bar propagation path, and the longitudinal displacement was obtained every 2 mm within 0.1 ms. Fig. 10 shows the various wave modes obtained from 0 to 150 kHz with the PCdisp results. The spectrogram summarizes three key points. First, the primary energy of the guided wave is concentrated around 70 kHz, and the phenomenon of dispersion prevents the effective extraction of a single mode. Meanwhile, a large number of PZT slices cannot be arranged to obtain the wave number in the actual structure. Second, the numerically and experimentally obtained signals are from these modes and not from the interface reflections. Third, the energy of L(0, 9) occupies a large proportion among the numerous modes. Therefore, these points show that the TR method of guided waves is highly advantageous for this structure.

Fig. 11 shows the reception diagram of the test piece (S1) in the experiment and the envelope obtained by Hilbert transform. The signal has multiple wave packets, and a certain amount of superposition occurs between each wave packet. Therefore, the waveform used for reversal is very important to the TR effect. The all-received signal need not be used for time reversal. On the one hand, some modes are insensitive to damage and consume a huge amount of memory and time. On the other hand, the TR process causes the guided wave to experience secondary damping loss, resulting in a small residual wave in the received signal, which has a weak influence on the reconstructed signal. For this reason, the previous work analyzed the optimal frequency to find the most suitable wave packet for TR, that is, L(0,9). The wave structure of L(0,9) is sensitive to grouting defects, and the speed is much higher than that of the second mode. The frequency–wavenumber analysis also confirms that the L(0,9) mainly exists in the propagation path. Even when seeking the optimal number of cycles, L(0,9) will theoretically be separated from the wave packets of the other modes. Given its dispersion phenomenon, L(0,9) will appear elongated in the time domain. Therefore, the first two wave packets are selected for TR to ensure that all L(0,9) waves return to the excitation point. The technology for automatic extremum identification determines the specific time point. Fig. 12(a) shows the received signal of the values of the four test pieces, and

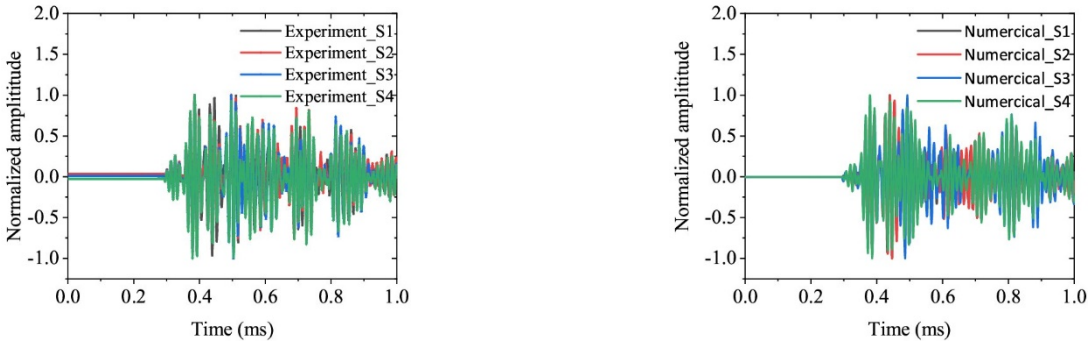

(a) Field test signal (b) Numerical signal

Fig. 12 The signal received by the sensor under different specimens of experiment and numerical

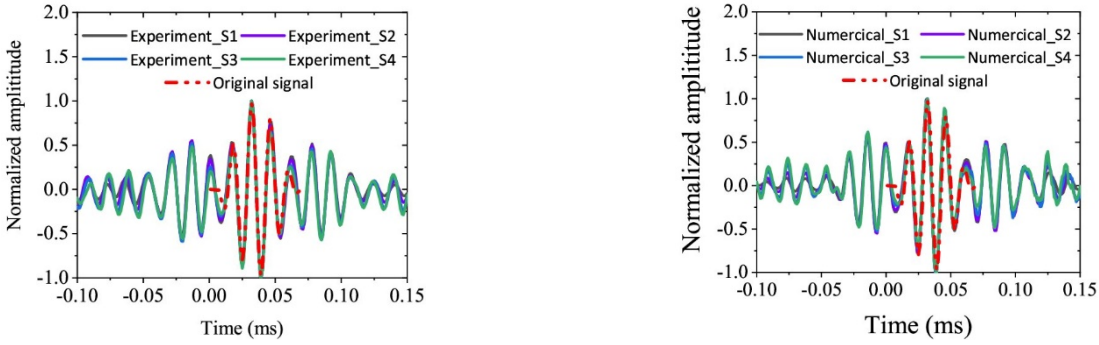

(a) Field test signal (b) Numerical signal

Fig. 13 The reconstructed signal received by the sensor under different specimens of experiment and numerical

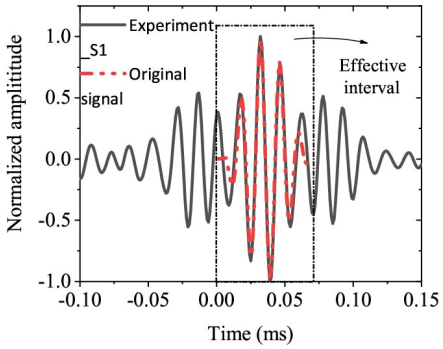

Fig. 14 Schematic diagram of extraction of effective time area of specimen S1

Fig. 12(b) presents the received response of the four test pieces in the field test. The selection method of the cut-off signal is the same as that of the test piece of S1. After cutting off the signals obtained from different specimens, they are re-acted on the excitation point.

4.3 Relationship between similarity and defecting

The signal received by the receiver for the second time is filtered in the time domain, and the time-reversed signal is corrected in time according to the start and end time of the time truncation window of the reversed signal. Fig. 13 shows the reconstructed signal diagrams of the experiment and numerical simulation, and the effective time area is the time width of the original excitation signal. The converted signal is extracted according to the effective interval of the original excitation signal to characterize the defect information, as shown in Fig. 14.

4.3.1 Damage identification based on time similarity

According to the definition of the TR coefficient in Section 1, the damping and frequency dependence of the grouting will destroy the invariance of TR, resulting in inconsistency between the correction and excitation signals. The lack of grouting avoids the leakage of the energy propagating along the steel bars, which will increase the similarity between the correction and excitation signals. To this end, a time-domain signal damage index (TDI) is constructed. The TDI is the most common evaluation index applied in the TR method. Meanwhile, the index meets the requirement that no baseline can improve the evaluation accuracy and does not require any comparison with the health signal, as shown in the following formula

$$TDI = \sqrt{\frac{\left(\int_{t0}^{t1} V_e(t) \cdot V_{tr}(t) \cdot dt\right)^2}{\int_{t0}^{t1} V_e(t) \cdot dt \cdot \int_{t0}^{t1} V_{tr}(t) \cdot dt}} \tag{18}$$

where $V_e(t)$is the excitation signal, and $V_{tr}(t)$ represent the time domain responses of the excitation signal and the reconstructed signal, respectively. The schematic diagram of their extraction process is shown in Fig. 14. $t0$ and $t1$

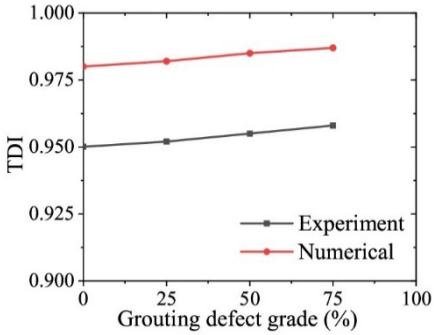

Fig. 15 The variation law of test and numerical TDI with the degree of grouting defects

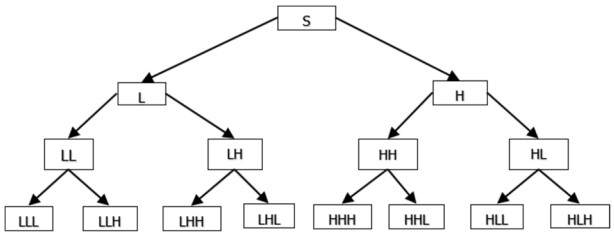

Fig. 16 Process diagram of wavelet packet decomposition

are the respective start and endpoints of the original excitation signal. The larger the TDI value is, the stronger the similarity between the signals is.

Fig. 15 shows the variation of the test and numerical TDI with the degree of grouting defects. The similarity coefficient is calculated according to Eq. (18). Before calculation, the original and reconstructed signals are normalized. The numerical value and the experimental indicators tend to increase with the grouting defect. However, the increase does not exceed 0.01, making the evaluation of the defect's size difficult. The sidelobe packets formed on both sides of the corrected signal will also cause uncertain factors. In addition, the grouting material has a strong scattering attenuation effect on the high-frequency part of the signal, causing the waveform to oscillate at the edge (Sohn *et al*. 2007). Therefore, a highly sensitive indicator for EGS grouting defects must be proposed.

4.3.2 Damage identification based on wavelet packet energy

The study of signal changes over time is called time-domain signal analysis. This type of analysis completely ignores the natural frequency of the structure. Fast Fourier transform is usually used for the frequency analysis of signals, but its shortcomings are due to the periodicity assumption of Fourier changes. To overcome the limitations of the two methods above, wavelet transform, which can deal with non-stationary signals well and eliminate of the periodicity assumption of Fourier transform, is proposed. However, wavelet analysis can only further process the low-frequency part but cannot decompose the high-frequency component. Wavelet packet analysis is based on wavelet transform while further decomposing the high-frequency portion of the signal (Stephane 1999). As shown in Fig.16, 'L' represents the low-frequency part of the signal, and 'H' represents the high-frequency component of the signal. The choice of the wavelet basis function should be similar to that of analyzing the signal waveform, so this article chooses the 'Demy' basis function for wavelet packet decomposition.

Given that the TR coefficient is affected by the damping and frequency dependence, the proportion of high-frequency components of the correction signal will increase with the grout defect level. For this reason, a new wavelet packet damage indicator (WDI) is proposed as

$$WDI = \sqrt{\frac{\left(\int_0^s E_a(t)\cdot E_{tr}(t)\cdot dt\right)^2}{\int_0^s E_a(t)\cdot dt\cdot\int_0^s E_{tr}(t)\cdot dt}} \tag{19}$$

where E_a and E_{tr} are the energies of each frequency band of the excitation signal and the reconstructed signal after wavelet packet decomposition, s is the number of nodes after wavelet packet decomposition. The lack of grouting will change the energy distribution in each frequency band. This indicator belongs to the category of no baseline and need not be compared with any baseline signal. As the level of grouting defects increases, the WDI will increase accordingly.

After the signal is sampled, the sampling frequency is 500 Khz, which satisfies the Shannon sampling theorem. At this time, the frequency range corresponding to the 0 node

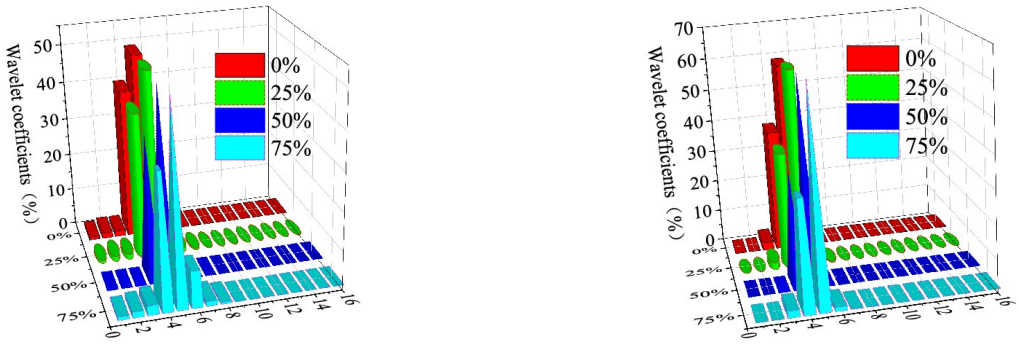

(a) Experimental signal (b) Numerical signal

Fig. 17 Wavelet packet energy distribution of experimental and numerical signal

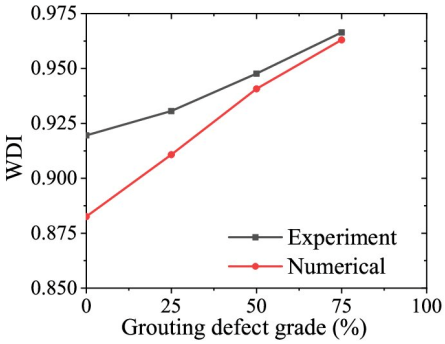

Fig. 18 The variation law of test and numerical WDI with the degree of grouting defects

is 0–250 kHz. The energy distribution of the corrected signal after the 4-layer wavelet packet decomposition is decipted in Fig. 17. The frequency width of each interval is 15.625 kHz. It can be seen that the proportion of frequency components of the signal will gradually change as the level of grouting defects increases. In addition, to better illustrate the impact of grouting material on the frequency band, the ratio of the relative high-frequency part (125–250 kHz) to the total spectrum was further extracted from Fig. 17, prior to the index evaluation. It was found that the ratio of the high-frequency part increased by 7% in the experimental signal, while it increased by 19% in the simulated signal, when the defect level rose from 0% to 75%. This phenomenon of high-frequency shift of the ultrasonic frequency band caused by the absence of cement-based materials has also been reported in Na *et al*. (2003).

According to Eq. (19), the WDI of different defect levels is calculated as shown in Fig. 18. The numerical and experimental WDI values approximately increase linearly with the grouting defect level. Therefore, the higher the grouting defect level is, the greater the WDI value is, and the waveletpacket energy index can reflect the degree of grouting defect well. However, the experimental result and the numerical analysis result do not match exactly, which may be due to the following factors: EVA foam was used as a surrogate for the grouting material and the defect in the experiment, but EVA changed shape under the compression of the surrounding grouting material, creating irregular defect boundaries that deviated from the finite element model; the ribs on the rebar were omitted in the numerical analysis model, which might alter the ultrasonic frequency band distribution; the rebar and concrete in the numerical model were assumed to be elastic, and their viscoelastic properties were not accounted for. Nevertheless, both WDI and TDI can faithfully reveal the trend of defect changes, and WDI index has a higher sensitivity.

5. Conclusions

The characteristics of the guided waves propagation in the EGS without and with grouting defects are systematically investigated in the present study using analytical, numerical, and experimental analyses to develop PZT-induced wave-based SHM methods for grouting defects. The traditional guided wave scheme is unsuitable for multi-inter structure because it has many modes, high attenuation, and dispersion, which directly complicate the guided wave signals and the signal's characteristics for damage identification. Therefore, a TR-based multi-mode focusing and dispersion automatic compensation technology is proposed to eliminate the multi-mode phase difference in the EGS. Four EGS specimens without and with different grouting defects are designed and experimentally investigated to prove the efficiency and practicality of the proposed method. The following conclusions can be drawn based on the experimental and numerical study.

- The finite size of the medium is considered for calculating the dispersion curve. The comparison of the numerical and experimental signals and the theoretical wave structure confirm that the approximate EGS model could effectively replace the full-scale three-dimensional model of the actual EGS. Therefore, the model is very cost-effective.
- The success of guided wave detection largely depends on the choice of wave mode. For this reason, numerical values, theoretical analysis, and experiments are combined to provide a set of optimal frequencies and cycles suitable for EGS structures. The wave packets that are sensitive to defects are found through Hilbert transform, and the TR operation is performed. The TR method can realize the multi-mode automatic focusing and dispersion compensation of guided waves, thereby eliminating the phase difference of different modes in the EGS.
- The conventional indicator of TR does not change significantly with the defects, so the WDI is proposed to reflect the frequency under different damage degrees. Wavelet packet analysis can avoid the inherent periodicity assumption of Fourier transform and decompose the signal at high frequency. The WDI decomposed by the $Demy$ wavelet four-layer can effectively evaluate the defect length in the numerical and experiment values. As the defect increases, the WDI value changes significantly. Meanwhile, the WDI does not require prior structural information, which is conducive for developing baseline-free damage identification for large structures.
- In this study, the EGS is in a stress-free state. Further research should focus on the method's applicability under complex stress states.

Acknowledgments

The authors are grateful for the financial support from the National Natural Science Foundation of China (NSFC) under Grant Nos. 52278294; the NSFCunder Grant Nos. 51778104; the National Key Research and Development Program of China (Project No. 2017YFC0703410)

References

Asadollahi, A. and Khazanovich, L. (2019), "Numerical investigation of the effect of heterogeneity on the attenuation of shear waves in concrete", *Ultrasonics*, **91**, 34-44. https://doi.org/10.1016/j.ultras.2018.07.011

Beard, M., Lowe, M. and Cawley, P. (2003), "Ultrasonic guided waves for inspection of grouted tendons and bolts", *J. Mater. Civil Eng.*, **15**(3), 212-218. https://doi.org/10.1061/(ASCE)0899-1561(2003)15:3(212)

Bocchini, P., Marzani, A. and Viola, E. (2011), "Graphical user interface for guided acoustic waves", *J. Comput. Civil Eng.*, **25**(3), 202-210. https://doi.org/10.1061/(ASCE)CP.1943-5487.0000081

De Barros, S., Gama, A.L., Rousseau, M. and Collet, B. (2004), "Characterization of bonded plates with Lamb and SH waves using a quasi-static approximation", *Latin Am. J. Solids Struct.*, **1**(4), 379-399.

Du, G., Kong, Q., Wu, F., Ruan, J. and Song, G. (2016), "An experimental feasibility study of pipeline corrosion pit detection using a piezoceramic time reversal mirror", *Smart Mater. Struct.*, **25**(3), 037002. https://doi.org/10.1088/0964-1726/25/3/037002

El Najjar, J. and Mustapha, S. (2020), "Understanding the guided waves propagation behavior in timber utility poles", *J. Civil Struct. Health Monitor.*, **10**, 793-813. https://doi.org/10.1007/s13349-020-00417-0

Fink, M. (1992), Time reversal of ultrasonic fields: Part I—Basic principles: IEEE Transactions on Ultrasonics, Ferroelectrics and Frequency Control, ITUCER.

Fröjd, P. and Ulriksen, P. (2017), "Frequency selection for coda wave interferometry in concrete structures", *Ultrasonics*, **80**, 1-8. https://doi.org/10.1016/j.ultras.2017.04.012

Gresil, M. and Giurgiutiu, V. (2015), "Prediction of attenuated guided waves propagation in carbon fiber composites using Rayleigh damping model", *J. Intell. Mater. Syst. Struct.*, **26**(16), 2151-2169. https://doi.org/10.1177/1045389X14549870

Guan, R., Lu, Y., Duan, W. and Wang, X. (2017), "Guided waves for damage identification in pipeline structures: A review", *Struct. Control Health Monitor.*, **24**(11), e2007. https://doi.org/10.1002/stc.2007

Hay, T.R. and Rose, J.L. (2002), "Flexible PVDF comb transducers for excitation of axisymmetric guided waves in pipe", *Sensors Actuators A: Phys.*, **100**(1), 18-23. https://doi.org/10.1016/S0924-4247(02)00044-4

Hong, X., Song, G., Ruan, J., Zhang, Z., Wu, S. and Liu, G. (2016), "Active monitoring of pipeline tapered thread connection based on time reversal using piezoceramic transducers", *Smart Struct. Syst., Int. J.*, **18**(4), 643-662. https://doi.org/10.12989/sss.2016.18.4.643

Huang, L., Zeng, L., Lin, J. and Luo, Z. (2018), "An improved time reversal method for diagnostics of composite plates using Lamb waves", *Compos. Struct.*, **190**, 10-19. https://doi.org/10.1016/j.compstruct.2018.01.096

Ing, R. and Fink, M. (1998), "Self-focusing and time recompression of Lamb waves using a time reversal mirror", *Ultrasonics*, **36**(1-5), 179-186. https://doi.org/10.1016/S0041-624X(97)00100-5

Kühn, M., Dobert, F. and Gessner, K. (2006), "Numerical investigation of the effect of heterogeneous permeability distributions on free convection in the hydrothermal system at Mount Isa, Australia", *Earth Planet. Sci. Lett.*, **244**(3-4), 655-671. https://doi.org/10.1016/j.epsl.2006.02.041

Li, D. and Liu, H. (2019), "Detection of sleeve grouting connection defects in fabricated structural joints based on ultrasonic guided waves", *Smart Mater. Struct.*, **28**(8), 085033. https://doi.org/10.1088/1361-665X/ab29b0

Li, Z., Zheng, L., Chen, C., Long, Z. and Wang, Y. (2019), "Ultrasonic detection method for grouted defects in grouted splice sleeve connector based on wavelet pack energy", *Sensors*, **19**(7), 1642. https://doi.org/10.3390/s19071642

Li, S., Liu, X., Ma, Y., Zhang, L. and Feng, H. (2021), "Influence of grouted sleeve and concrete strength of fabricated shear wall on acoustic emission detection method for sleeve compactness", *J. Build. Eng.*, **43**, 102541. https://doi.org/10.1016/j.jobe.2021.102541

Liu, H., Qi, Y., Chen, Z., Tong, H., Liu, C. and Zhuang, M. (2021), "Ultrasonic inspection of grouted splice sleeves in precast concrete structures using elastic reverse time migration method", *Mech. Syst. Signal Process.*, **148**, 107152. https://doi.org/10.1016/j.ymssp.2020.107152

Ma, Y., Li, S., Wu, Y., Wang, D. and Liu, M. (2019), "Acoustic emission testing method for the sleeve grouting compactness of fabricated structure", *Constr. Build. Mater.*, **221**, 800-810. https://doi.org/10.1016/j.conbuildmat.2019.06.124

Michaels, T.E., Michaels, J.E. and Ruzzene, M. (2011), "Frequency–wavenumber domain analysis of guided wavefields", *Ultrasonics*, **51**(4), 452-466. https://doi.org/10.1016/j.ultras.2010.11.011

Mitra, M. and Gopalakrishnan, S. (2016), "Guided wave based structural health monitoring: A review", *Smart Mater. Struct.*, **25**(5), 053001. https://doi.org/10.1088/0964-1726/25/5/053001

Mustapha, S., Ye, L., Wang, D. and Lu, Y. (2012), "Debonding detection in composite sandwich structures based on guided waves", *AIAA J.*, **50**(8), 1697-1706. https://doi.org/10.2514/1.J051274

Mustapha, S., Lu, Y., Li, J. and Ye, L. (2014), "Damage detection in rebar-reinforced concrete beams based on time reversal of guided waves", *Struct. Health Monitor.*, **13**(4), 347-358. https://doi.org/10.1177/1475921714521268

Na, W.B., Kundu, T. and Ehsani, M.R. (2003), "Lamb waves for detecting delamination between steel bars and concrete", *Comput.-Aided Civil Infrastr. Eng.*, **18**(1), 58-63. https://doi.org/10.1111/1467-8667.t01-1-00299

Philippidis, T. and Aggelis, D. (2005), "Experimental study of wave dispersion and attenuation in concrete", *Ultrasonics*, **43**(7), 584-595. https://doi.org/10.1016/j.ultras.2004.12.001

Planes, T. and Larose, E. (2013), "A review of ultrasonic Coda Wave Interferometry in concrete", *Cement Concrete Res.*, **53**, 248-255. https://doi.org/10.1016/j.cemconres.2013.07.009

Qiu, L. and Yuan, S. (2011), "A phase synthesis time reversal impact imaging method for on-line composite structure monitoring", *Smart Struct. Syst., Int. J.*, **8**(3), 303-320. https://doi.org/10.12989/sss.2011.8.3.303

Rose, J. (2014), *Ultrasonic waves in solid media*, Cambridge University Press, Cambridge, UK.

Saitoh, T. and Ishiguro, A. (2021), "Surface crack detection in a thin plate using time reversal analysis of SH guided waves", *Struct. Eng. Mech., Int. J.*, **80**(3), 243-251. https://doi.org/10.12989/sem.2021.80.3.243

Seco, F. and Jiménez, A.R. (2012), "Modelling the generation and propagation of ultrasonic signals in cylindrical waveguides", *Ultrasonic Waves*, 1-28.

Sohn, H., Park, H.W., Law, K.H. and Farrar, C.R. (2007), "Combination of a time reversal process and a consecutiv outlier analysis for baseline-free damage diagnosis", *J. Intell. Mater. Syst. Struct.*, **18**(4), 335-346. https://doi.org/10.1177/1045389X0606629

Stephane, M. (1999), *A wavelet tour of signal processing*, Elsevier

Su, Z., Ye, L. and Lu, Y. (2006), "Guided Lamb waves for identification of damage in composite structures: A review", *J. Sound Vib.*, **295**(3-5), 753-780. https://doi.org/10.1016/j.jsv.2006.01.020

Sun, H. and Zhu, J. (2020), "Nondestructive evaluation of steel-

concrete composite structure using high-frequency ultrasonic guided wave", *Ultrasonics*, **103**, 106096. https://doi.org/10.1016/j.ultras.2020.106096

Sutin, A., Johnson, P. and TenCate, J. (2003). "Development of nonlinear time reversed acoustics (NLTRA) for applications to crack detection in solids", *Proceedings of the 5th World Congress on Ultrasonics*.

Tullini, N. and Minghini, F. (2016), "Grouted sleeve connections used in precast reinforced concrete construction–Experimental investigation of a column-to-column joint", *Eng. Struct.*, **127**, 784-803. https://doi.org/10.1016/j.engstruct.2016.09.021

Wang, Q., Yuan, S., Hong, M. and Su, Z. (2015), "On time reversal-based signal enhancement for active lamb wave-based damage identification", *Smart Struct. Syst., Int. J.*, **15**(6), 1463-1479. https://doi.org/10.12989/sss.2015.15.6.1463

Wilcox, P., Lowe, M. and Cawley, P. (2001), "The effect of dispersion on long-range inspection using ultrasonic guided waves", *NDT & E Int.*, **34**(1), 1-9. https://doi.org/10.1016/S0963-8695(00)00024-4

Wu, D., Liang, S., Guo, Z., Zhu, X. and Fu, Q. (2016), "The development and experimental test of a new pore-forming grouted precast shear wall connector", *KSCE J. Civil Eng.*, **20**, 1462-1472. https://doi.org/10.1007/s12205-015-0071-3

Xu, K., Ta, D., Moilanen, P. and Wang, W. (2012), "Mode separation of Lamb waves based on dispersion compensation method", *J. Acoust. Soc. Am.*, **131**(4), 2714-2722. https://doi.org/10.1121/1.3685482

Xue, C., Su, C., Yu, M., Xu, H. and Ye, J. (2021), "Experimental Study on the Thermal-Mechanical Properties and Degradation of Sleeve Grouting Material at Elevated Temperatures", *J. Mater. Civil Eng.*, **33**(2), 04020453. https://doi.org/10.1061/(ASCE)MT.1943-5533.0003493

Yao, F., Ji, Y., Tong, W., Li, H.X. and Liu, G. (2021), "Sensing technology based quality control and warning systems for sleeve grouting of prefabricated buildings", *Automat. Constr.*, **123**, 103537. https://doi.org/10.1016/j.autcon.2020.103537

Zhang, Y., Li, D. and Zheng, X. (2019), "Detection and location of bolt group looseness using ultrasonic guided wave", *Smart Struct. Syst., Int. J.*, **24**(3), 293-301. https://doi.org/10.12989/sss.2019.24.3.293

Zhang, W., Wang, J., Zhang, J., Cao, Y., Qin, P. and Yi, W. (2020), "Experimental study on post-fire performance of half grouted sleeve connection with construction defect", *Constr. Build. Mater.*, **244**, 118165. https://doi.org/10.1016/j.conbuildmat.2020.118165

Zheng, M., Ma, H., Lyu, Y., He, C. and Lu, C. (2019), "On the dispersion of cylinder guided waves propagating in a multilayer composite hollow cylinder made of anisotropic materials", *Aerosp. Sci. Technol.*, **95**, 105432. https://doi.org/10.1016/j.ast.2019.105432

Zhu, Y., Zeng, X., Deng, M., Han, K. and Gao, D. (2018), "Detection of nonlinear Lamb wave using a PVDF comb transducer", *Ndt & E Int.*, **93**, 110-116. https://doi.org/10.1016/j.ndteint.2017.09.012